Thermoelectric properties of Heusler Fe_2TiSn alloys

Hiroshi Nakatsugawa[1, *], Toshiki Ozaki[1], Hiroaki Kishimura[2], and Yoichi Okamoto[2]

[1] *Yokohama National University, 79-5 Tokiwadai, Hodogaya-Ku, Yokohama 240-8501, Japan*

[2] *National Defense Academy, 1-10-20 Hashirimizu, Yokosuka 239-8686, Japan*

[*] Corresponding Author: naka@ynu.ac.jp

Abstract

It is commonly believed that reducing the thermal conductivity of Heusler alloys is important for improving their thermoelectric properties. In this study, we focused on Fe_2TiSn, which exhibits a relatively low thermal conductivity among Heusler alloys, to investigate the advantages of a powder metallurgy method that can easily form samples of desired shapes and produce dense samples with less segregation. We prepared sintered Fe_2TiSn specimens using powders milled in air or Ar for 1, 3, and 12 h. We found that varying the non-stoichiometric composition led to deviations from the Fe_2TiSn content of samples milled in air as a result of the appearance of a second phase, and the temperature at which the Seebeck coefficient changes from *p*-type to *n*-type decreased with increasing milling time for samples milled in air. For samples milled in Ar, no change in the Seebeck coefficient with milling time was observed. Although no significant difference was found between the electrical resistivities and thermal conductivities of samples milled in air and Ar, increasing the milling time promoted phonon scattering at the grain boundaries and reduced the lattice thermal conductivity. We determined a maximum dimensionless figure of merit (*ZT*) of 0.0014 at 285 K for the Fe_2TiSn alloy milled in Ar for 3 h.

(Received: XX/XX/2019; Accepted: XX/XX/2019; Published online: XX/XX/2019)

Keywords:

thermoelectric properties, Heusler alloy, sintered sample, milling time, ZT value

1. Introduction

Thermoelectric power generation is a technology for directly converting thermal energy into electrical energy. Since most energy that is not used in an energetic process and discarded is thermal energy, it is possible to more effectively utilize energy by converting unused thermal energy into electrical energy through thermoelectric power generation. In particular, Heusler alloys, represented by Fe_2VAl, composed of abundant elements and having relatively low toxicity, have attracted attention as candidates for thermoelectric materials. These alloys promise to play an important role in sustainable societies of the future.

A Heusler alloy is an intermetallic compound having a chemical composition of X_2YZ with an $L2_1$ structure and, in general, transition elements for the X and Y atoms and group 13, 14, or 15 elements for the Z atom [1]. A Heusler alloy loses its magnetism when the valence electron concentration (VEC) per chemical composition is 24 [2, 3]. There is a pseudogap in which the conduction band and valence band state densities slightly overlap near the Fermi level when the VEC per atom is 6 [4]. The pseudogap has been confirmed by X-ray photoelectron spectroscopy [5], the photoelectric effect [6], nuclear magnetic resonance [7, 8], the Hall effect [9], and first-principles calculations [10-17]. Owing to the pseudogap, a Heusler alloy behaves as a semimetal that exhibits semiconductive behavior, even though it is a metal, so that the Seebeck coefficient S of the metal can be approximated by Mott's theory [18], i.e.,

$$S = -\frac{\pi^2}{3}\frac{k_B{}^2 T}{e}\frac{1}{N(E_F)}\left[\frac{\partial N(E)}{\partial E}\right]_{E=E_F}, \qquad (1)$$

where k_B is the Boltzmann constant, e is the elementary charge, and $N(E_F)$ is the density of states at the Fermi level. As can be inferred from Eq. (1), a high S can be achieved by a small

density of states and a large energy gradient at the Fermi level. In the band structure with a pseudogap, the density of states at the Fermi level is very small and the energy gradient of the density of states near the Fermi level exhibits a sharp increase, so a high S can be achieved in a Heusler alloy by controlling the Fermi level. Nishino *et al.* [19] have reported that a high S (80 μVK^{-1} for p-type and -130 μVK^{-1} for n-type) can be attained by substituting various fourth elements in the Heusler alloy Fe_2VAl. In particular, $Fe_2VAl_{0.9}Si_{0.1}$, in which 10% of the Al sites are substituted by Si, has an n-type power factor as high as 5400 $\mu Wm^{-1}K^{-2}$ at 300 K [20]. Since the power factor of Bi_2Te_3 [21], which has been used as a thermoelectric material, is 4000 to 5000 $\mu Wm^{-1}K^{-2}$, a Heusler alloy can be said to have an equally high potential as a thermoelectric material like Bi_2Te_3. However, reducing the thermal conductivity κ is important for improving the thermoelectric characteristics of Heusler alloys represented by Fe_2VAl.

Although Heusler alloys of various compositions have been studied to date, there are few reports on other Fe_2VAl. For example, Lue *et al.* [22] reported that the electrical resistivity ρ and the Seebeck coefficient S are very sensitive to the non-stoichiometry of $Fe_{2-x}Ti_{1+x}Sn$, and S = 27.5 μVK^{-1} for Fe_2TiSn (x = 0.0) at 300 K. Yabuuchi *et al.* [23] predicted from first-principles calculations that Fe_2TiSi and Fe_2TiSn would exhibit a high n-type S from -300 to -160 μVK^{-1} around 300 K when electron carriers are added at a concentration from 1×10^{20} to 1×10^{21} cm^{-3}. The optimal VECs per chemical composition for Fe_2TiSi and Fe_2TiSn to realize a high power factor $S^2\rho^{-1}$ are around 24.05 and 24.06, respectively [23]. These results suggest that $Fe_2TiSn_{1-x}Si_x$ alloys have great potential to realize a higher dimensionless figure of merit $ZT = S^2T\rho^{-1}\kappa^{-1}$ value, as compared to conventional Heusler alloys typified by Fe_2VAl. Moreover, Voronin *et al.* reported κ = 7–8 $Wm^{-1}K^{-1}$ for Fe_2TiSn at 300 K [24], which is considerably lower than the κ = 25 $Wm^{-1}K^{-1}$ for Fe_2VAl reported by Murawski *et al.* [25], the latter being roughly seven times larger

than that of Bi_2Te_3-based thermoelectric materials [21]. These are the reasons why we focused on Fe_2TiSn in this study. Furthermore, if sintered bodies can be prepared by the powder metallurgy method, phonon scattering increases owing to crystal grain refinement, which should reduce κ [26-28]. This study also investigated the powder metallurgy method, which can easily form the desired shape and produce a dense sample with less segregation. A sintered body with a stoichiometric composition of Fe_2TiSn, which shows a relatively low κ among Heusler alloys, was produced using a mechanically homogenized powder by adjusting the milling time and atmosphere. In particular, we improved the thermoelectric characteristics of Fe_2TiSn alloys by controlling the grain refinement, promoting phonon scattering at the crystal grain boundaries, and reducing κ.

2. Experimental

Fe_2TiSn ingot samples were prepared from stoichiometric quantities of Fe (99.99% purity), Ti (99% purity), and Sn (99.9% purity), melted with an arc melting furnace (NEV-AD 60L-S300, Nissin Giken) under an Ar atmosphere. Six types of Fe_2TiSn powders were prepared by milling in air or Ar for 1, 3, and 12 h at 1080 rpm using ⌀5 mm stainless steel balls. Fe_2TiSn sintered bodies were obtained by wet mixing the powder using methanol, press forming into pellets at 12 MPa, calcining for 2 h at 723 K under a 4-Pa vacuum, vacuum sealing in a quartz tube, and sintering at 1073 K for 48 h.

The microstructure of the samples was observed using a scanning electron microscope (SEM) (VE-8800, KEYENCE). The particle size distribution and average particle diameter of the samples were analyzed using ImageJ [29]. Energy dispersive X-ray spectrometry (EDS) and

energy dispersive X-ray (EDX) analysis (SU8010, HITACHI-HIGHTECH) were used for qualitative and quantitative chemical composition analyses of the samples, respectively. The non-stoichiometric compositions of the samples were estimated from the average values of EDX point analyses measured at 20 points.

Powder X-ray diffraction (XRD) data were measured with a diffractometer (SmartLab, Rigaku) using the CuKα (λ = 1.542 Å) line. The crystal structure parameters were refined by Rietveld analysis using the software RIETAN-FP [30] on the XRD data measured at 2θ = 10 to 90° with a scanning step of 0.02°. The relative density of each sample was calculated from the ratio between the density measured by the Archimedes method and the ideal density refined by Rietveld analysis.

ρ and S were measured by the steady method and dc four-probe method, respectively, using a ResiTest 8300 (Toyo Co., Ltd.) in the temperature range from 80 to 395 K. κ was measured using a power conversion efficiency measurement apparatus (PEM-2, ULVAC-RIKO) between 305 and 415 K. This is why the measurement temperatures were different for ρ, S, and κ. Since, as described below, the sample density was too low to evaluate the accuracy of the thermoelectric properties, the relative density was used to correct the experimental values of ρ and κ. However, no such correction was made to the experimental value of S.

3. Results and Discussion

Figure 1 shows the results of Rietveld analysis obtained using RIETAN-FP [30] on the XRD data of samples milled in (a) air and (b) Ar for 1 h, where the crystal structure parameters of

first-phase Fe_2TiSn are refined using the $L2_1$ ordered structure (space group: *Fm-3m*, No. 225) and those of second-phase FeSn are refined using the hexagonal structure (space group: *P6/mmm*, No. 191). As shown in Fig. 1, the second phase of the sample milled in Ar for 1 h is considerably suppressed compared to that of the sample milled in air for 1 h. The crystal structure parameters of six specimens milled in air and Ar for 1, 3, and 12 h are summarized in Tables 1 and 2. Table 1 shows the result of Rietveld analysis considering only the first phase, while Table 2 shows that of Rietveld analysis considering both the first and second phases. In the samples milled for 1 h, the reliability factor R_{wp} weighted to the R profile was 8.454% in air and 5.578% in Ar when considering only the first phase and 5.279% in air and 5.245% in Ar when considering both the first and second phases. In the samples milled for 3 h, R_{wp} was 6.856% in air and 4.430% in Ar, considering only the first phase, whereas for the first and second phases, R_{wp} was 6.129% in air and 4.798% in Ar. In the samples milled for 12 h, R_{wp} was 6.430% in air and 5.498% in Ar for the first phase, and for the first and second phases, R_{wp} was 4.181% in air and 5.114% in Ar. R_{wp} improved dramatically by considering both the first and second phases in any specimen milled in air, whereas the specimens milled in Ar showed no significant change in R_{wp} or even deteriorated when considering both the first and second phases. These results strongly suggest that for the samples milled in Ar, the formation of the second phase was suppressed, while the second phase is formed in only small amounts in the samples milled in air.

The relative densities, which were calculated from the ratio between the density measured by the Archimedes method and the ideal density refined by Rietveld analysis, were 85.8, 86.7, 86.4, 87.0, 86.6, and 87.0% for the samples milled in air for 1 h, in Ar for 1 h, in air for 3 h, in Ar for 3 h, in air for 12 h, and in Ar for 12 h, respectively.

Figure 2 shows SEM fractographs of the six types of samples milled in air and Ar for 1, 3, and 12 h. Figure 3 shows the particle size distribution and average particle size for each sample, determined from the SEM images in Fig. 2 using ImageJ [29]. Figs. 2 and 3 show that the sample milled in air for 1 h had an average particle size of 0.86 μm, whereas the sample milled for 12 h had a finer average particle size of 0.69 μm. It was found that as the milling time increased, the particle size distribution narrowed, i.e., the particle diameter became more uniform. Similarly, in the sample milled in Ar for 1 h, the average grain size was 0.88 μm, whereas in the sample milled for 12 h, the average grain size was lower (0.66 μm). As the milling time increased, the particle size distribution narrowed, i.e., the particle diameter became more uniform, as for the samples milled in air.

Figures 4 (a) and (b) show the results of qualitative chemical composition analyses obtained through SEM-EDS for the samples milled in air and Ar for 3 h. Figure 4(a) confirms the segregation of Fe, Ti, and Sn, and a deviation from the stoichiometric composition due to the second phase is expected for the sample surface milled in air. On the other hand, as seen in Fig. 4(b), it is expected that the constituent elements will be mixed uniformly in a substantially stoichiometric composition on the sample surface milled in Ar. Table 3 tabulates the results of quantitative chemical composition analyses obtained by SEM-EDX for samples milled in air and Ar for 1, 3, and 12 h. In particular, the variation of non-stoichiometric composition is greater for samples milled in air than for samples milled in Ar. In fact, the chemical composition of a sample milled in air for 3 h is $Fe_{2.0(2)}Ti_{1.0(4)}Sn_{1.0(2)}$; i.e., VEC is expected to be in the range of 5.1 to 6.9. In contrast, the chemical composition of a sample milled in Ar for 3 h is $Fe_{2.07(6)}Ti_{1.00(8)}Sn_{0.94(5)}$; i.e., VEC is expected to be in the range of 5.8 to 6.4.

Figure 5 shows the temperature dependence of S for each sample in the temperature range from 80 to 395 K. In the samples milled in air, S changes from p-type to n-type as the temperature increases, but as the milling time changes from 3 to 12 h, the temperature-induced change from p-type to n-type shifts to lower temperatures. This is considered to be due to the variation in non-stoichiometric composition. As shown in Table 3, the chemical composition changes from $Fe_{2.0(2)}Ti_{1.0(4)}Sn_{1.0(2)}$ ($5.1 \leqq VEC \leqq 6.9$) to $Fe_{1.9(2)}Ti_{1.2(2)}Sn_{0.94(7)}$ ($5.3 \leqq VEC \leqq 6.5$) as the milling time is increased from 3 to 12 h. Variations in VEC are suppressed and the offsetting S of the p-type and n-type is promoted. Thus, it is to be expected that the temperature-induced change from p-type to n-type will shift to lower temperatures as the milling time changes from 3 to 12 h. On the other hand, in the samples milled in Ar, no change in S with milling time could be confirmed. As shown in Fig. 5, the S of samples milled in Ar shows a maximum around 160K, and $S = 15 \mu VK^{-1}$ at 300K. Although the maximum value of S is shown at around 400 K, the value of S at 300 K is in good agreement with the results reported by Lue *et al.*[22] As shown in Table 3, the chemical composition of samples milled in Ar are $Fe_{2.05(5)}Ti_{1.00(8)}Sn_{0.94(7)}$ ($5.9 \leqq VEC \leqq 6.3$) for the sample milled for 1 h, $Fe_{2.07(6)}Ti_{1.00(8)}Sn_{0.94(5)}$ ($5.8 \leqq VEC \leqq 6.4$) for the sample milled for 3 h, and $Fe_{2.01(7)}Ti_{1.09(8)}Sn_{0.90(3)}$ ($5.8 \leqq VEC \leqq 6.2$) for the sample milled for 12 h. These findings suggest that the deviation from the stoichiometric composition of Fe_2TiSn is slightly suppressed in the samples milled in Ar as compared to those milled in air.

Figure 6 shows the temperature dependence of ρ corrected by relative density for each sample in the temperature range from 80 to 395 K. There is no significant difference in ρ between the samples milled in air and those milled in Ar, although the temperature dependence of ρ for each sample does not correspond to the intrinsic conduction because no thermal activation occurs in this temperature range. This suggests that the variation of non-stoichiometric composition due

to the appearance of the second phase resulting from the shift in the stoichiometric composition of Fe_2TiSn is not sufficient to affect ρ. The inset shows the temperature dependence of normalized electric resistivity $\rho(T)$ / ρ(300K) for each sample. On the basis of the results of temperature dependence of the normalized electrical resistivity of $Fe_{2-x}Ti_{1+x}Sn$ ($-0.05 \leqq x \leqq 0.10$) reported by Lue *et al.*[22], it is understood that the temperature dependence of ρ for samples milled in air and in Ar falls at the boundary between metallic and semiconducting characteristics.

Figure 7 shows the temperature dependence of the power factor $S^2\rho^{-1}$ corrected by relative density for each sample in the temperature range from 80 to 395 K. Compared to the samples milled in air, the $S^2\rho^{-1}$ values for samples milled in Ar exhibit a dramatic increase. In particular, in samples milled in Ar, the formation of the second phase, the deviation from the stoichiometric Fe_2TiSn composition, and the decrease in $|S|$ are all suppressed. Thus, $S^2\rho^{-1}$ = 60 $\mu Wm^{-1}K^{-2}$ at 170 K for the sintered sample milled in Ar for 1 h is the maximum power factor value.

Figure 8 shows the temperature dependence of κ corrected by relative density for each sample in the temperature range from 305 to 415 K. The solid lines represent the quadratic least-squares approximation curves. κ decreased with increasing milling time and was, for example, 5.83 $Wm^{-1}K^{-1}$ at 305 K for the sample milled in air for 12 h. This is a reduction of about 25% compared to 7–8 $Wm^{-1}K^{-1}$, the κ reported for Fe_2TiSn by Voronin *et al.* [24] However, since no significant change in κ was observed in the sample milled for 12 h as compared to the sample milled for 3 h, it is considered that a milling treatment of about 3 h is sufficient for the crystal grain refinement process to reduce the thermal conductivity. Furthermore, no significant change

in κ was observed between the samples milled in air and Ar, so that changes in the electron system did not greatly influence κ.

Figure 9 shows the temperature dependence of the carrier thermal conductivity κ_{car} corrected by relative density for each sample calculated from the Wiedemann-Franz rule:

$$\kappa_{car} = \frac{L_0 T}{\rho} \tag{2}$$

in the temperature range from 305 to 415 K. The Lorenz number L_0 is defined as [31]

$$L_0 = \left(\frac{k_B}{e}\right)^2 \left[\frac{\left(r+\frac{7}{2}\right)F_{r+\frac{5}{2}}(\eta)}{\left(r+\frac{3}{2}\right)F_{r+\frac{1}{2}}(\eta)} - \left\{ \frac{\left(r+\frac{5}{2}\right)F_{r+\frac{3}{2}}(\eta)}{\left(r+\frac{3}{2}\right)F_{r+\frac{1}{2}}(\eta)} \right\}^2 \right], \tag{3}$$

where r is the scattering parameter, which is -0.5, because the acoustic phonon scattering was assumed to be the main carrier scattering mechanism, $\eta = \frac{E_F}{k_B T}$ is the reduced Fermi energy E_F, and $F_n(\eta) = \int_0^\infty \frac{\chi^n}{1+\exp(\chi-\eta)} d\chi$ is the n-th order Fermi integral. To determine the true Lorenz number, η should be calculated from its relationship with S, which is given as [31]

$$S = \pm \frac{k_B}{e} \left[\frac{\left(r+\frac{5}{2}\right)F_{r+\frac{3}{2}}(\eta)}{\left(r+\frac{3}{2}\right)F_{r+\frac{1}{2}}(\eta)} - \eta \right], \tag{4}$$

where η was determined by fitting the experimental value of S at each temperature with Eq. (4).

Figure 10 shows the temperature dependence of the lattice thermal conductivity $\kappa_{ph} = \kappa - \kappa_{car}$ corrected by relative density for each sample. As shown in Fig. 10, the κ for Fe_2TiSn alloys consists largely of κ_{ph}. κ_{ph} decreases by about 40% in the samples milled for 3 or 12 h, relative

to the sample milled for 1 h. Since there is little change in κ_{car}, it is considered that the reduction of κ_{ph} is due to phonon scattering at the grain boundary being promoted by grain refinement.

Figure 11 shows the temperature dependence of $ZT = S^2T\rho^{-1}\kappa^{-1}$ for each sample in the temperature range from 80 to 395 K, where the temperature dependence of κ was derived from the quadratic least-squares approximation curve in Fig. 8. The ZT values of samples milled in Ar are much larger than those of samples milled in air. In particular, in samples milled in Ar, the formation of the second phase, the deviation from the stoichiometric Fe_2TiSn composition, and the decrease of $|S|$ are suppressed, and the reduction of κ_{ph} is achieved by grain refinement. Thus, the ZT value of 0.0014, obtained at 285 K for the sample milled in Ar for 3 h, is the maximum ZT value.

4. Conclusion

Fe_2TiSn alloys were prepared from six kinds of powders, milled in air and Ar for 1, 3, and 12 h, and the crystal structure, microstructure, and thermoelectric properties were determined. In the samples milled in air, the second phase was formed only in small amounts, while the formation of the second phase was suppressed in samples milled in Ar. With increasing milling time, the particle size distribution narrowed, i.e., the grain size became more uniform. In samples milled in air, the Fe_2TiSn composition shifted as a result of the variation of the non-stoichiometric composition due to the appearance of the second phase, and the temperature at which S changed from p-type to n-type decreased as the milling time increased. However, samples milled in Ar showed no change in S with milling time. On the other hand, although no significant change was observed in ρ and κ between samples milled in air and Ar, phonon

scattering was promoted at the grain boundaries and reduction of κ_{ph} was confirmed as the milling time increased. The *ZT* value of 0.0014 obtained at 285 K for the sintered sample milled in Ar for 3 h was the maximum *ZT* value. Improving the thermoelectric properties of Fe_2TiSn alloys further requires more research using ingots or dense sintered samples with high relative density and suppressed non-stoichiometric composition variations.

Acknowledgments

The room-temperature XRD measurements and the microstructural characterization by SEM, EXS, and EDX were conducted using SmartLab, VE-8800, and SU8010 at the Yokohama National University Instrumental Analysis Evaluation Center. Melting of the samples using an arc melting furnace and measurements of the thermal conductivity above room temperature were carried out using NEV-AD 60L-S300 and PEM-2 at the National Defense Academy.

REFERENCES

1. H.C.Kandpal, G.H.Fecher, and C.Felser, J.Phy. D, **40**, 1507 (2007).
2. T.Graf, C.Felser, and S.S.P. Parkin, Progress in Solid State Chemistry, **39**, 1 (2011).
3. I.Galanakis and P. H. Dederichs, Condensed Matter and Material Physics, **66**, 1 (2002).
4. Y.Nishino, Mater. Trans., **42**, 902 (2001).
5. K. Soda, T. Mizutani, O. Yoshimoto, S. Yagi, U. Mizutani, H. Sumi, Y. Nishino, Y. Yamada, T. Yokoya, S. Shin, A.Sekiyama, and S. Suga, J. Synchrotron Rad., **9**, 233 (2002).
6. H. Okamura, J. Kawahara, T. Nanba, S. Kimura, K. Soda, U. Mizutani, Y. Nishino, M. Kato, I. Shimoyama, H. Miura, K. Fukui, K. Nakagawa, H. Nakagawa, and T. Kinoshita, Phys. Rev. Lett., **84**, 3674 (2000).
7. C.S. Lue and J.H. Ross, Jr., Phys. Rev. B, **58**, 9763 (1998).
8. C.S. Lue and J.H. Ross, Jr., Phys. Rev. B, **61**, 9863 (2000).
9. M. Kato, Y. Nishino, S. Asano, and S. Ohara, J. Japan Inst. Metals, **62**, 669 (1998).
10. D.I.Bilc, G.Hauitier, D.Waroquiers, G.Rignanese, and P.Ghosez, Phys. Rev. Lett., **114**, 136601 (2015).
11. T.Zou, T.Jia, W.Xie, Y.Zhang, M.Widenmeyer, X.Xiao, and A.Weidenkaff, Phys. Chem. Chem. Phys., **19**, 18273 (2017).
12. J.Jong, J.Yan, J.Zhu, and C.Kim, J. Electronic. Mater., **46**, 6038 (2017).
13. D.P.Rai, Sandeep, A.Shankar, R.Khenata, A.H.Reshak, C.E.Ekuma, R.K.Thapa, and S.Ke, AIP. Advance, **7**, 045118 (2017).
14. I.H.Bhat, T.M.Bhat, and D.C.Gupta, and J. Supercond, Novel. Magn, **31**, 3263 (2018) .
15. Y.Terasawa, M.Mikami, T.Itoh, and T.Takeuchi, J. Japan Inst. Metals, **76**, 216 (2012).
16. G.Y.Guo, G.A.Botton, and Y.Nishino, J. Phys. Rev.: Condens. Matter, **10**, 119 (1998).
17. A.Bansil, S.Kaprzyk, P.E.Mijnarends, and J.Tobola, Phys. Rev. B., **60**, 13396 (1999).
18. N.F.Mott and H.jones, *The Theory of the Properties of Metal* (Clarendon Press, Oxford,1936).
19. Y. Nishino, Materia Japan, **44**, 648 (2005).
20. H. Kato, M. Kato, Y. Nishino, U. Mizutani, and S. Asano, J. Japan Inst. Metals, **65**, 652 (2001).
21. B.Poudel, Q.Hao, Y.Ma, Y.Lan, A.Minnich, B.Yu, X.Yan, D.Wang, A.Muto, D.Vashaee, X.Chen, J.Liu, M.S.Dresselhaus, G.Chen, and Z.Ren, Science, **320**, 634 (2008).
22. C.S.Lue and Y.K.Kuo, J. Appl. Phys., **96**, 2681 (2004)

23. S.Yabuuchi, M.Okamoto, A.Nishide, Y.Kurosaki, and J.Hayakawa, Appl. Phys. Expr., **6**, 025504 (2013).
24. A.I.Voronin, V.Y. Zueva, D.Y.Karpenkov, D.O.Moskovskikh, A.P.Novitskii, H.Miki, and V.V.Khovaylo, Semiconductors, **51**, 891 (2017).
25. L.Murawski, C.H.Chung, and J.D.Mackenzie, J.non-crystalline Solids **32**, 91 (1970).
26. S.Katsuyama and T.Kobayashi, Mater. Sci. ENG. B, **166**, 99 (2010).
27. S.Katsuyama, F.Maezawa, and T.Tanaka, J.Jpn.Soc.Powder Powder Metallurgy, **58**, 99 (2011).
28. S.Katsuyama and T.Tanaka, J.Jpn.Soc.Powder Powder Metallurgy, **60**, 66 (2013).
29. C.T.Rueden, J.Schindelin, M.C.Hiner, B.E.Dezonia, A.E.Walter, E.T.Arena, and K.W.Eliceiri, BMC Bioinformatics. **18**, 529 (2017).
30. F.Izumi and K.Momma, Solid State Phenom. **130,** 15 (2007).
31. L.D.Zhao, S.H.Lo, J.Q.He, H.Li, K.Biswas, J.Androulakis, C.I.Wu, T.P.Hogan, D.Y.Chung, V.P.Dravid, and M.G.Kanatzidis, J.Am.Chem.Soc., **133**, 20476 (2011).

Figure captions

Fig. 1 Powder XRD patterns of Fe_2TiSn alloys milled (a) in air for 1 h and (b) in Ar for 1 h.

Fig. 2 SEM images of Fe_2TiSn alloys milled in air for (a) 1 h, (b) 3 h, and (c) 12 h, and in Ar for (d) 1 h, (e) 3 h, and (f) 12 h.

Fig. 3 Particle size distribution and average particle size of Fe_2TiSn alloys milled in air for (a) 1 h, (b) 3 h, and (c) 12 h, and in Ar for (d) 1 h, (e) 3 h, and (f)12 h.

Fig. 4 Chemical composition qualitative analyses using SEM-EDS of Fe_2TiSn alloys milled (a) in air for 3 h and (b) in Ar for 3 h.

Fig. 5 Temperature dependence of S for Fe_2TiSn alloys.

Fig. 6 Temperature dependence of ρ corrected by relative density for Fe_2TiSn alloys, where the inset shows temperature dependence of normalized ρ.

Fig. 7 Temperature dependence of $S^2\rho^{-1}$ corrected by relative density for Fe_2TiSn alloys.

Fig. 8 Temperature dependence of κ corrected by relative density for Fe_2TiSn alloys, where the solid lines represent quadratic least-squares approximation curves.

Fig. 9 Temperature dependence of κ_{car} corrected by relative density for Fe_2TiSn alloys, where the inset shows temperature dependence of L_0 determined by Eq. (3).

Fig. 10 Temperature dependence of κ_{ph} corrected by relative density for Fe_2TiSn alloys.

Fig. 11 Temperature dependence of ZT for Fe_2TiSn alloys.

Table captions

Table 1 Crystal structure parameters of Fe_2TiSn alloys.

Table 2 Crystal structure parameters of Fe_2TiSn alloys and the 2nd phase of FeSn.

Table 3 Non-stoichiometric composition and VEC of Fe_2TiSn alloys.

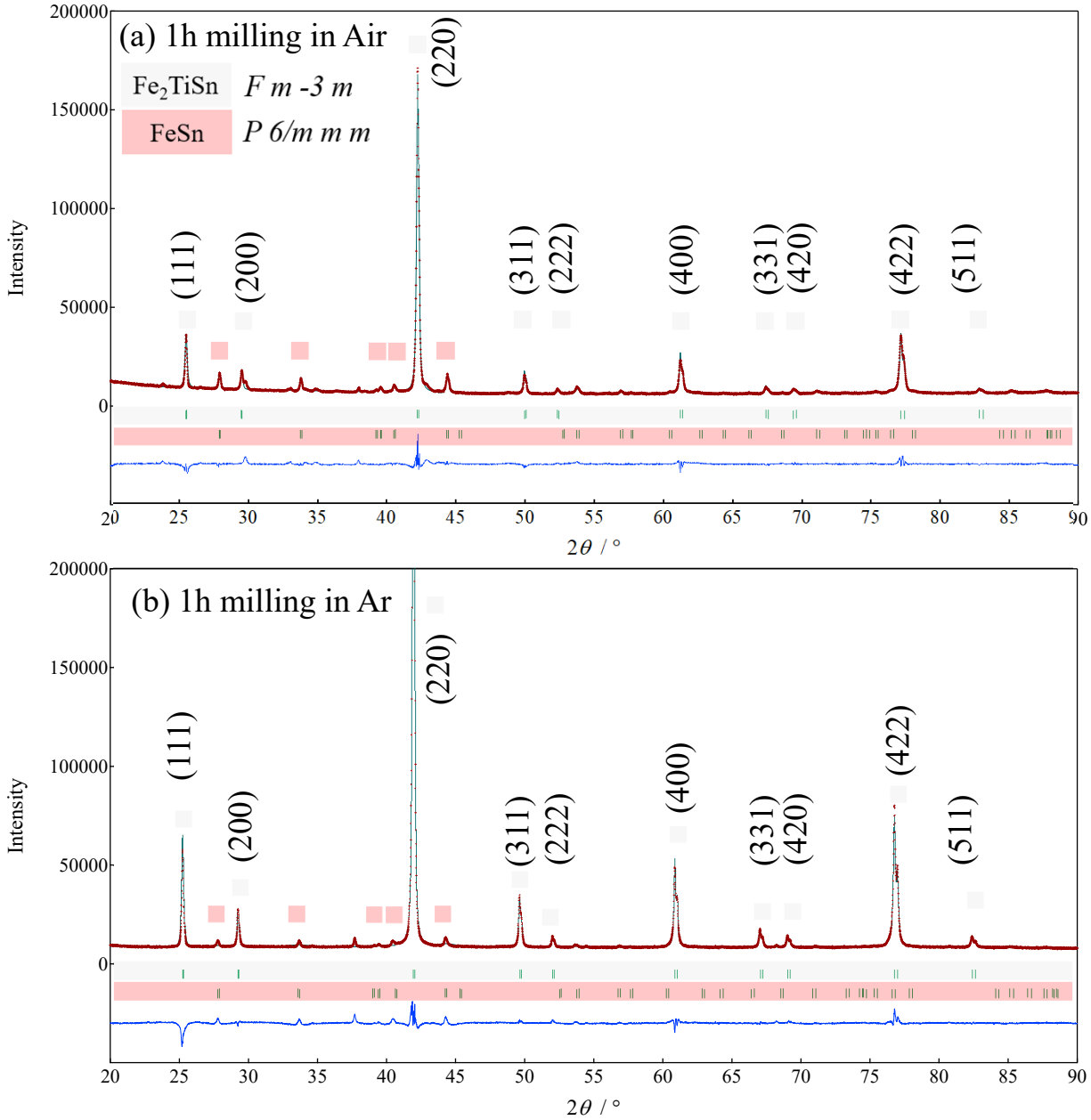

Fig. 1 Powder XRD patterns of Fe_2TiSn alloys milled (a) in air for 1 h and (b) in Ar for 1 h.

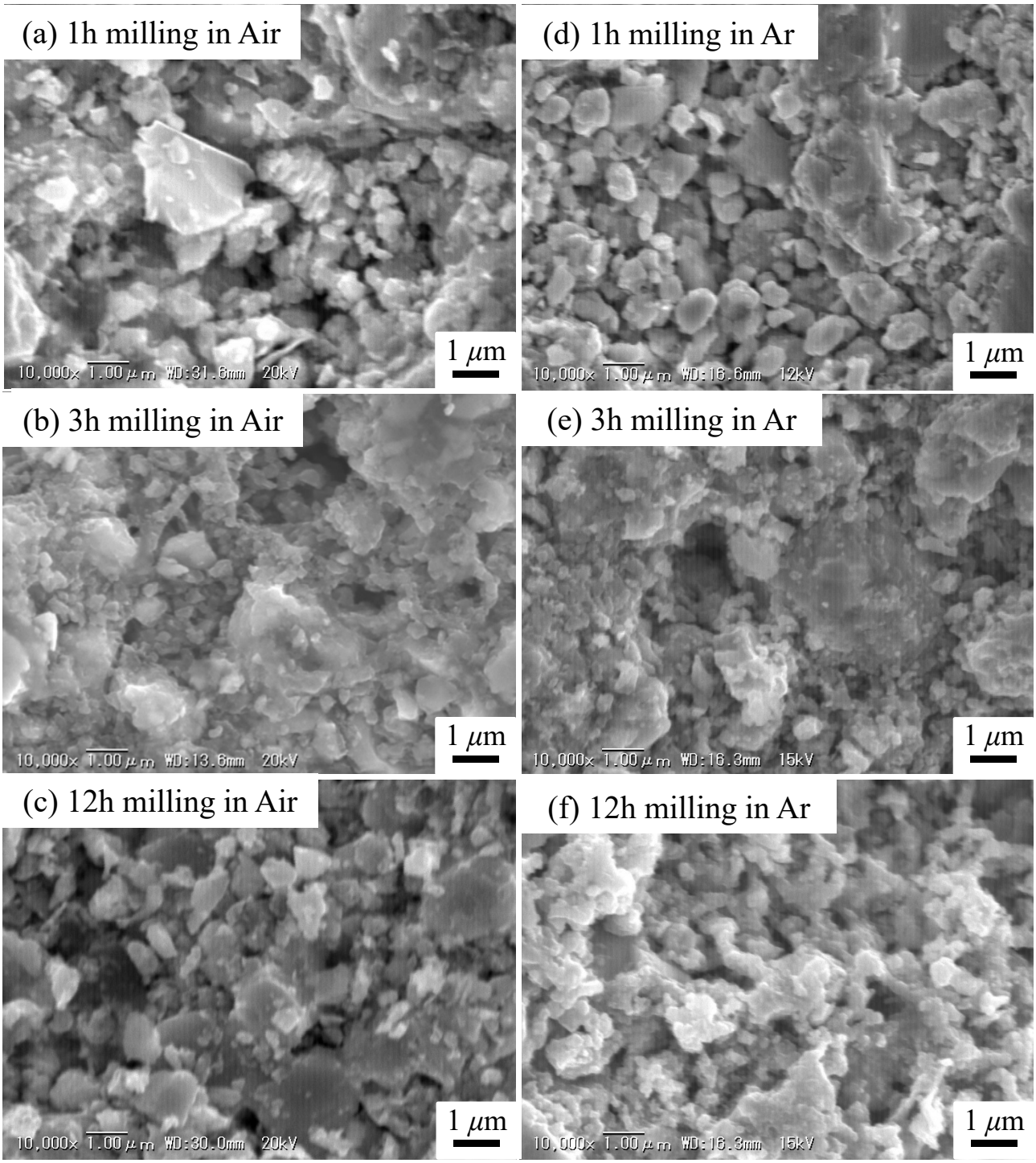

Fig. 2 SEM images of Fe_2TiSn alloys milled in air for (a) 1 h, (b) 3 h, and (c) 12 h, and in Ar for (d) 1 h, (e) 3 h, and (f) 12 h.

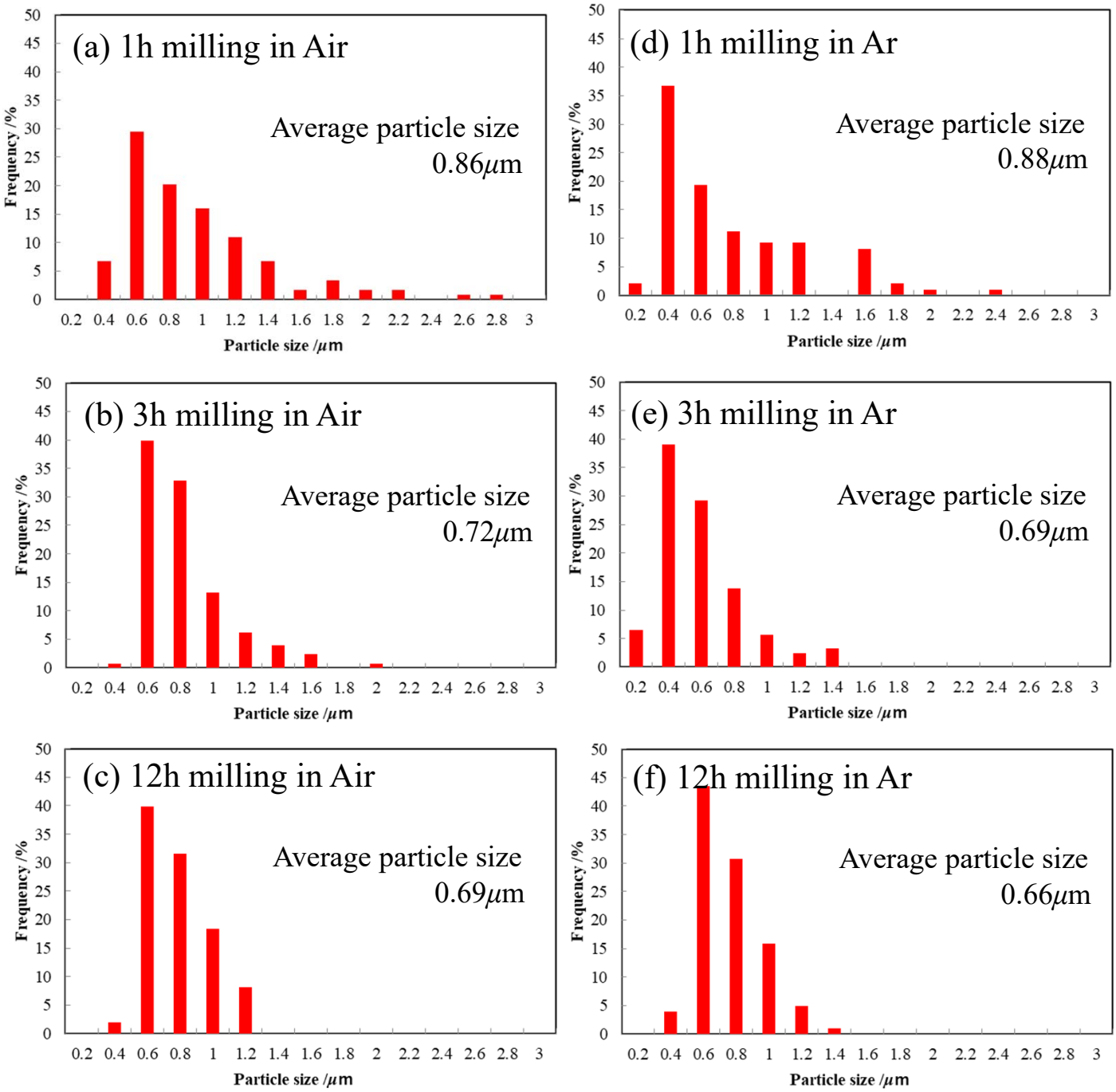

Fig. 3 Particle size distribution and average particle size of Fe_2TiSn alloys milled in air for (a) 1 h, (b) 3 h, and (c) 12 h, and in Ar for (d) 1 h, (e) 3 h, and (f)12 h.

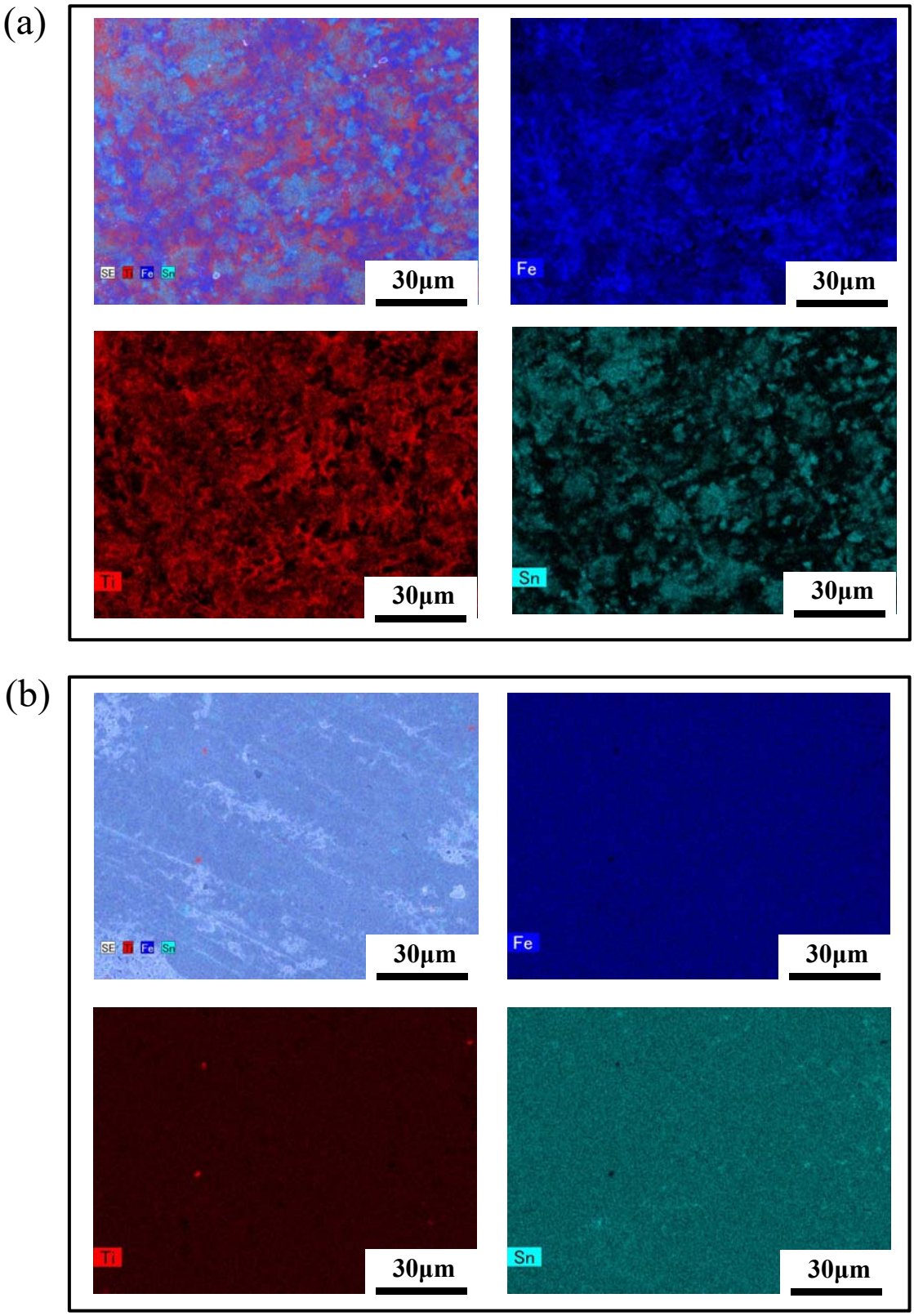

Fig.4 Chemical composition qualitative analyses using SEM-EDS of Fe_2TiSn alloys milled (a) in air for 3 h and (b) in Ar for 3 h.

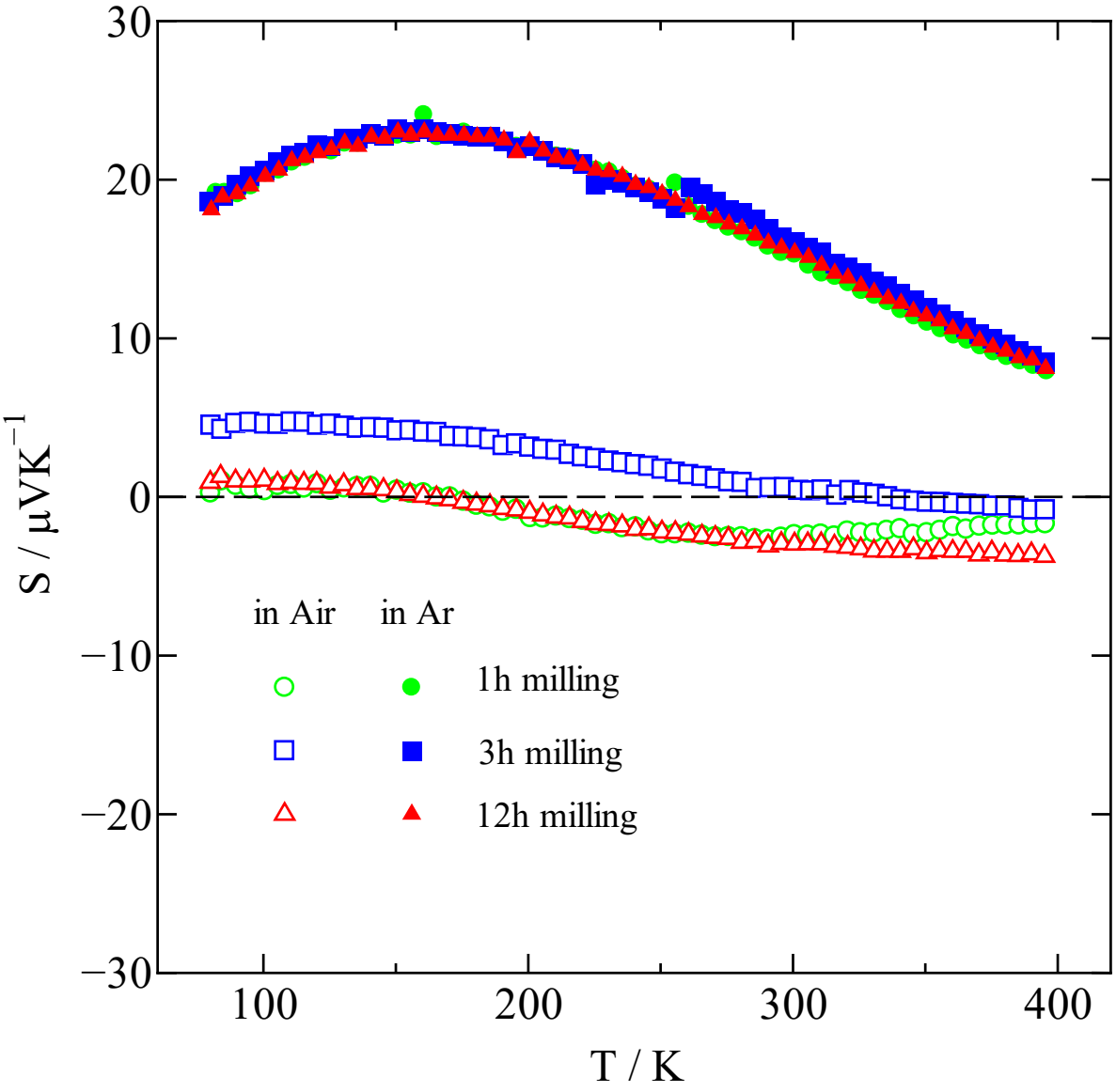

Fig. 5 Temperature dependence of S for Fe_2TiSn alloys.

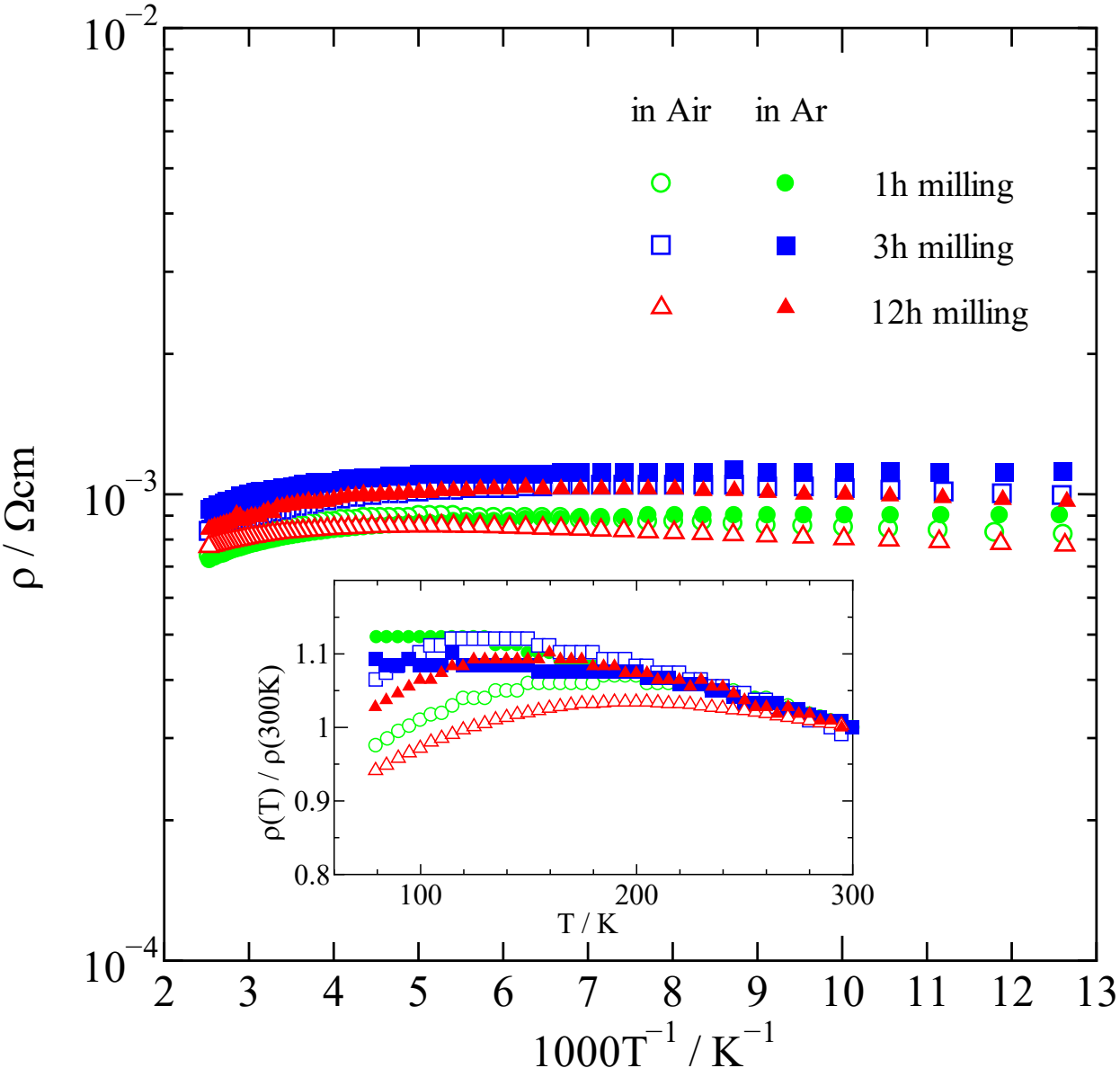

Fig. 6 Temperature dependence of ρ corrected by relative density for Fe_2TiSn alloys, where the inset shows temperature dependence of normalized *ρ*.

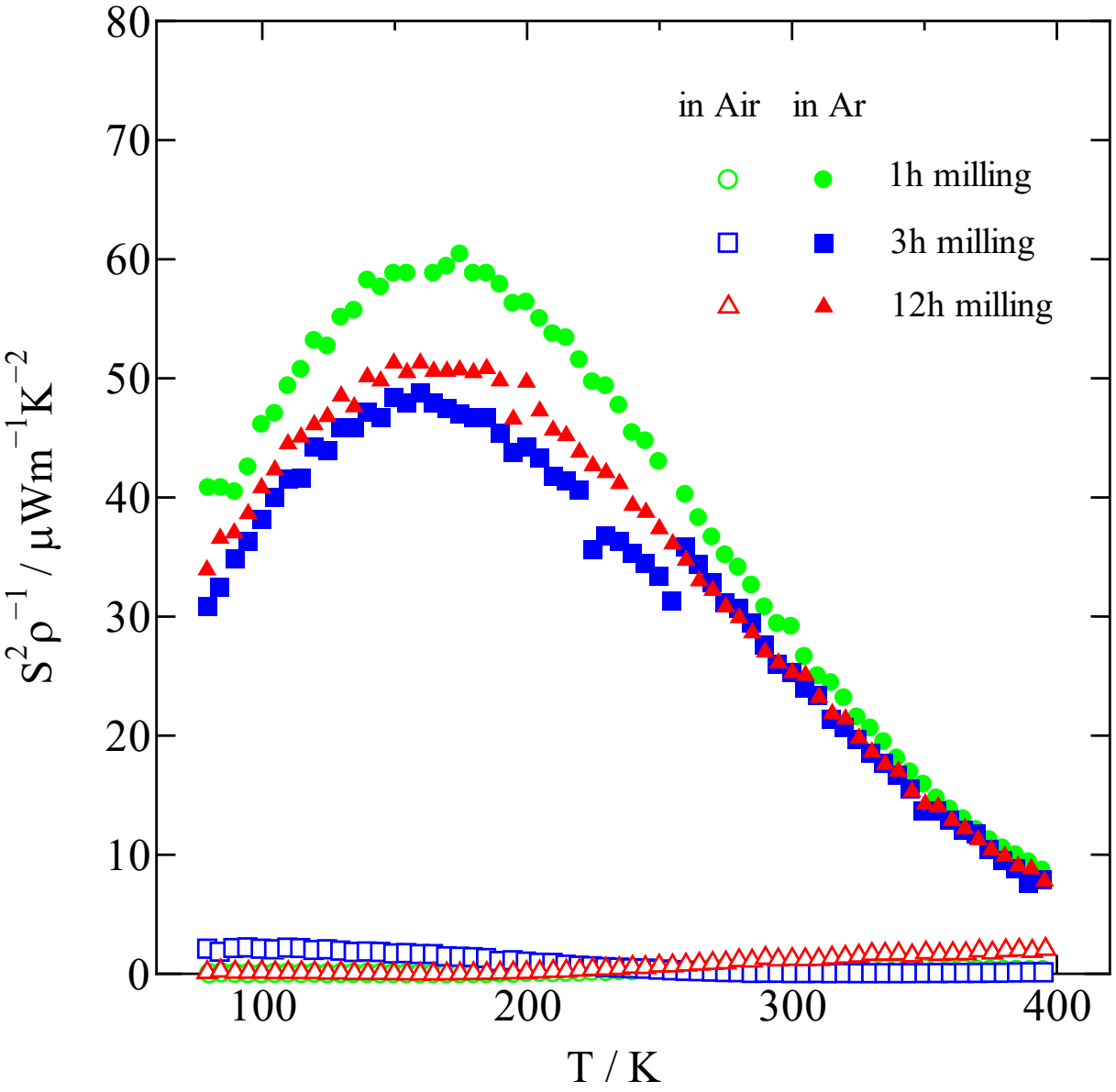

Fig. 7 Temperature dependence of $S^2\rho^{-1}$ corrected by relative density for Fe_2TiSn alloys.

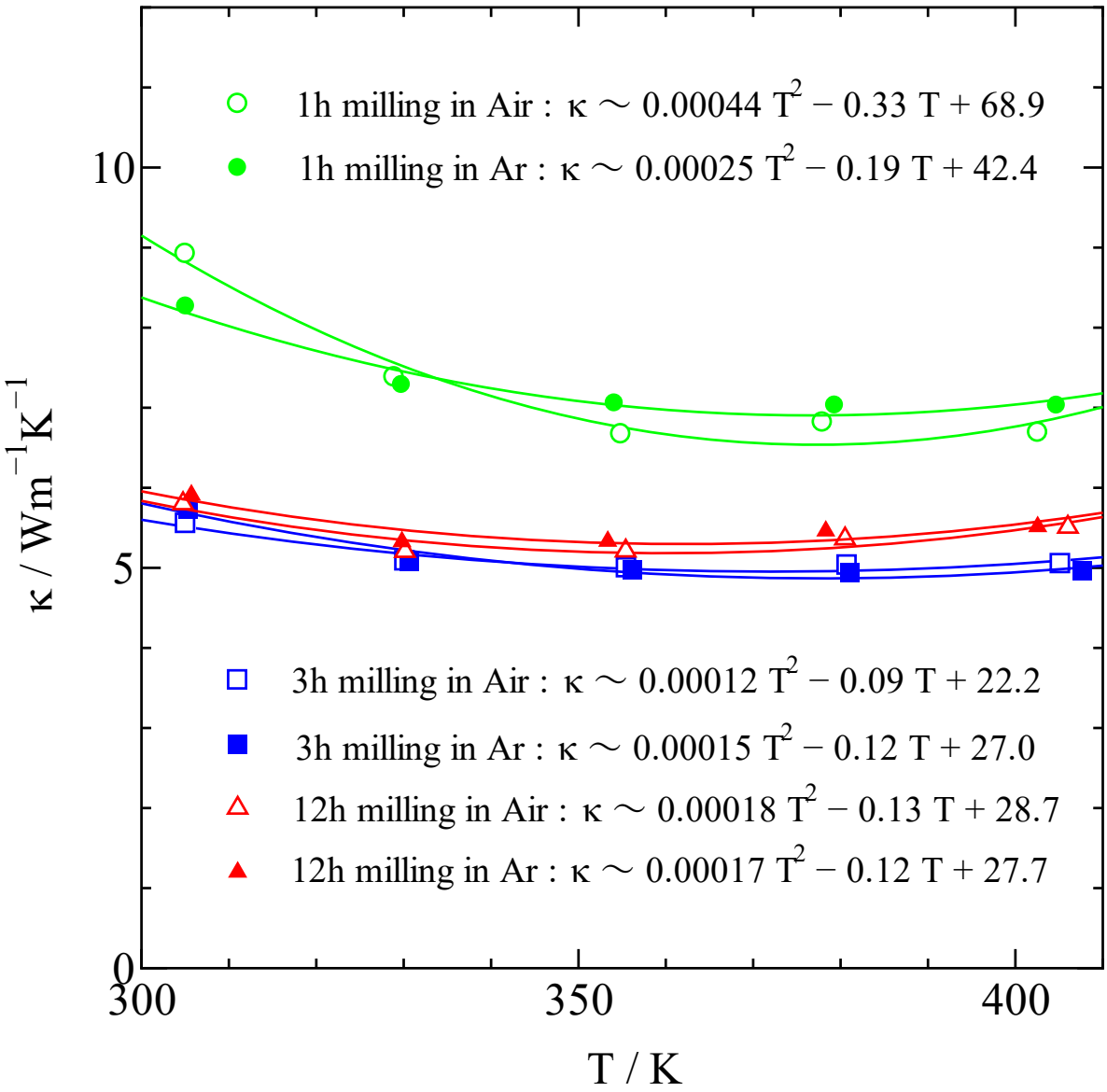

Fig. 8 Temperature dependence of κ corrected by relative density for Fe_2TiSn alloys, where the solid lines mean quadratic least square approximation curves.

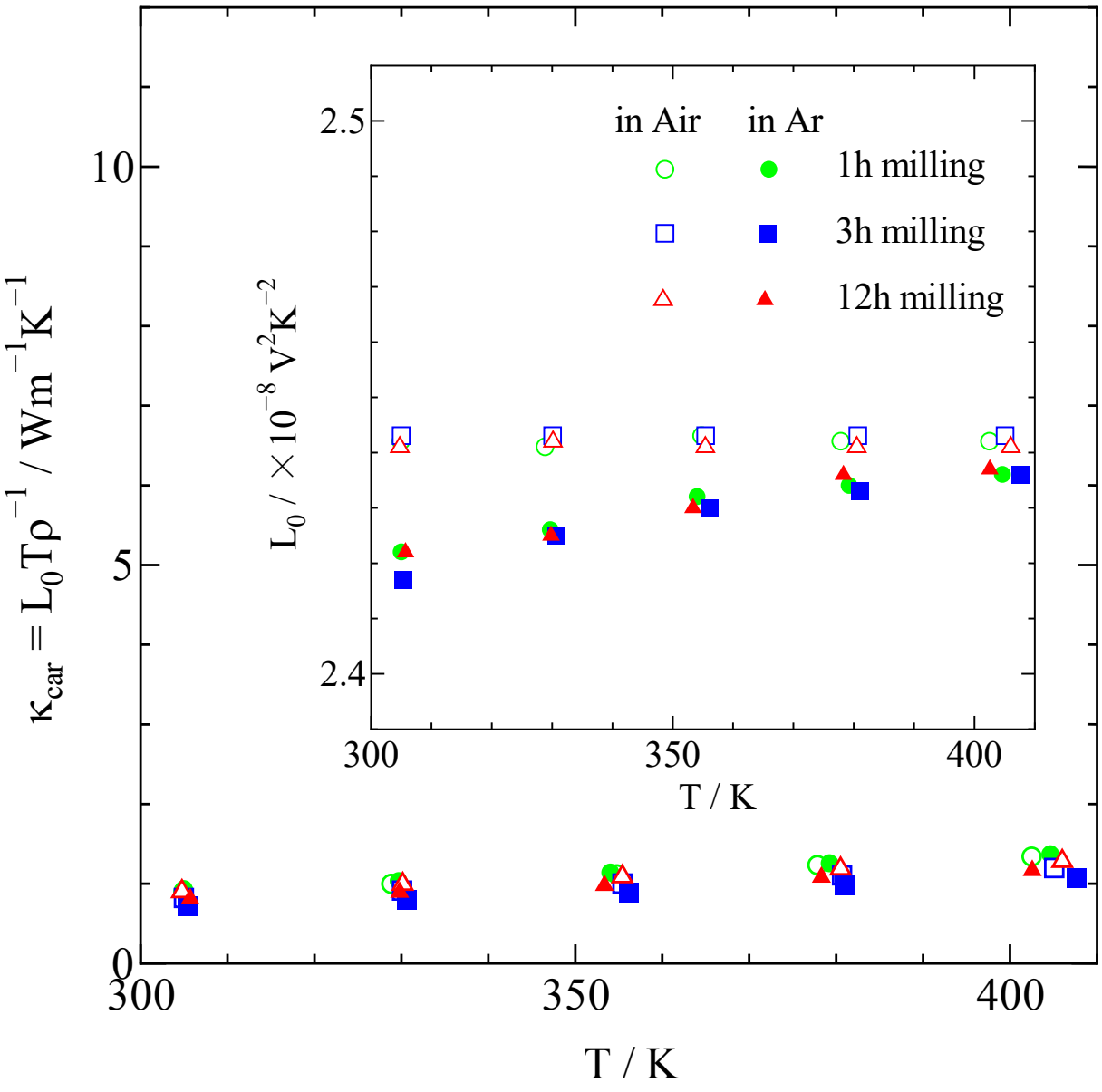

Fig. 9 Temperature dependence of κ_{car} corrected by relative density for Fe_2TiSn alloys, where the inset shows temperature dependence of L_0 determined by Eq.(3).

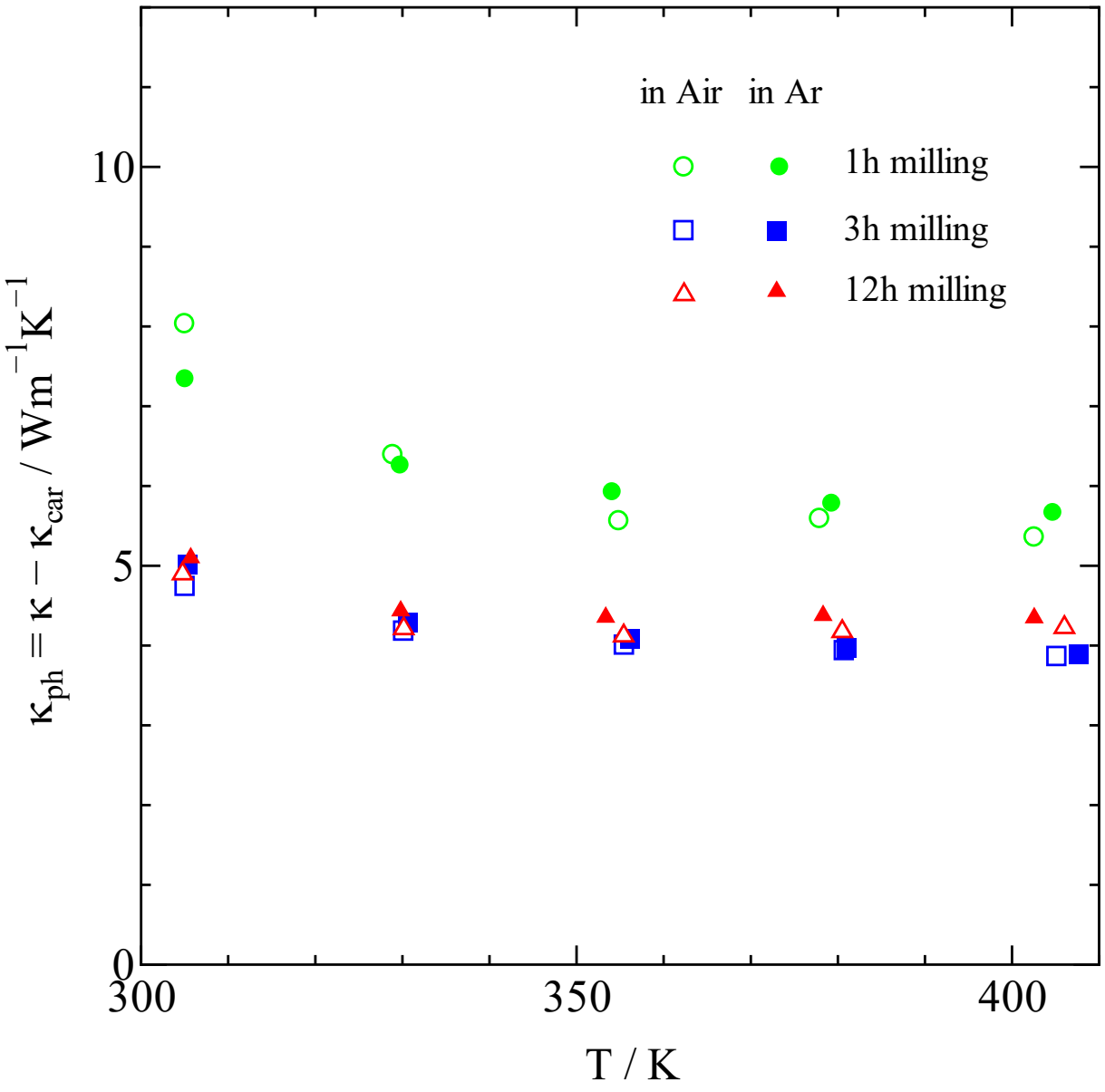

Fig. 10 Temperature dependence of κ_{ph} corrected by relative density for Fe_2TiSn alloys.

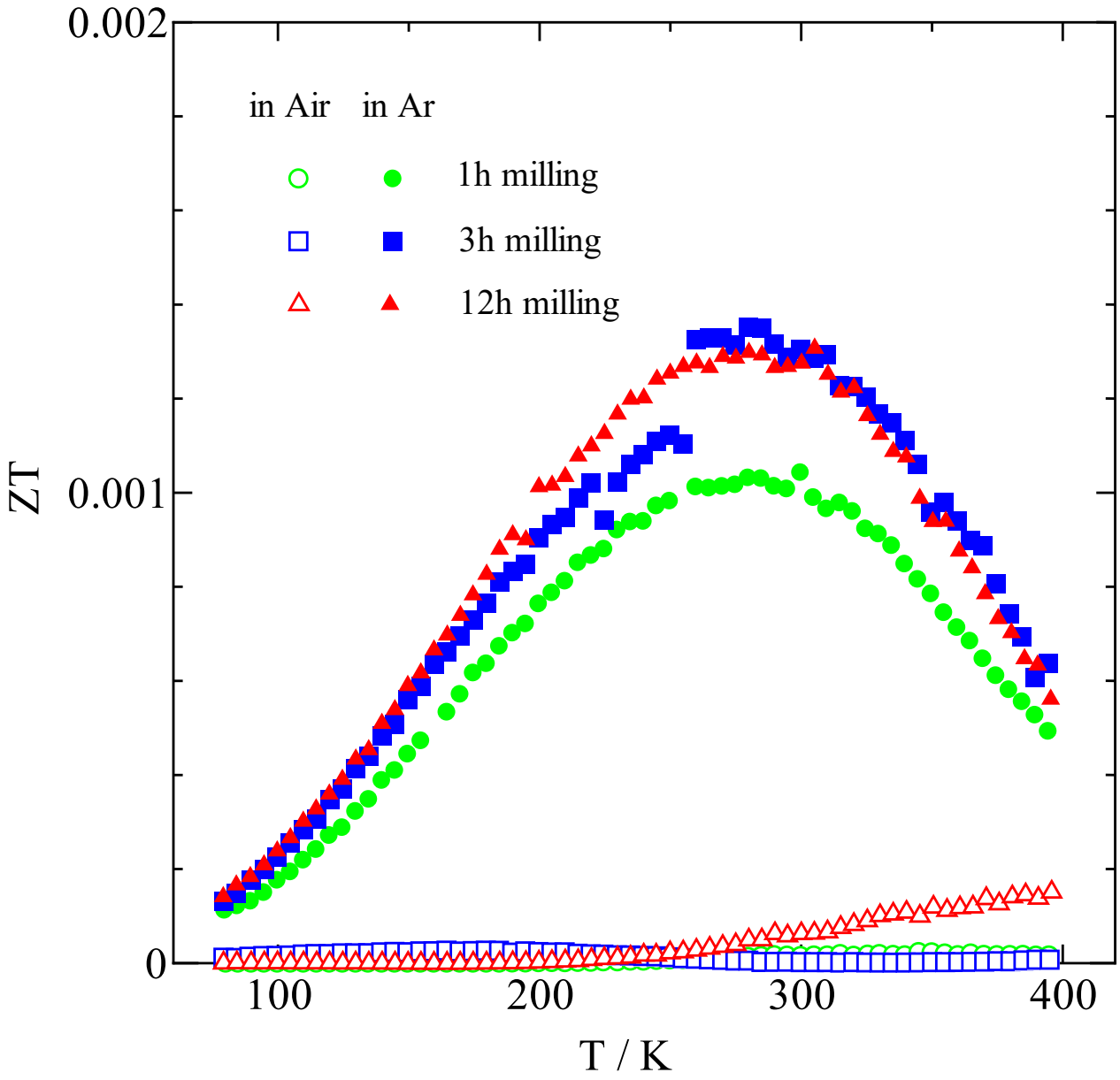

Fig. 11 Temperature dependence of *ZT* for Fe_2TiSn alloys.

Table.1 Crystal structure parameters of Fe_2TiSn alloys.

milling time		1h in Air	1h in Ar	3h in Air	3h in Ar	12h in Air	12h in Ar
the 1st phase		Fe_2TiSn					
space group		*Fm-3m*	*Fm-3m*	*Fm-3m*	*Fm-3m*	*Fm-3m*	*Fm-3m*
a (Å)		6.0478(2)	6.0675(4)	6.0679(4)	6.0712(2)	6.0683(3)	6.0728(7)
b (Å)		6.0478(2)	6.0675(4)	6.0679(4)	6.0712(2)	6.0683(3)	6.0728(7)
c (Å)		6.0478(2)	6.0675(4)	6.0679(4)	6.0712(2)	6.0683(3)	6.0728(7)
α(deg.)		90	90	90	90	90	90
β(deg.)		90	90	90	90	90	90
γ(deg.)		90	90	90	90	90	90
V (Å^3)		221.20(6)	223.37(6)	223.42(1)	223.77(3)	223.46(4)	223.96(6)
Fe	x	1/4	1/4	1/4	1/4	1/4	1/4
	y	1/4	1/4	1/4	1/4	1/4	1/4
	z	1/4	1/4	1/4	1/4	1/4	1/4
	B (Å^2)	0.5	0.5	0.5	0.5	0.5	0.5
	g	1.0	1.0	1.0	1.0	1.0	1.0
Ti	x	1/2	1/2	1/2	1/2	1/2	1/2
	y	1/2	1/2	1/2	1/2	1/2	1/2
	z	1/2	1/2	1/2	1/2	1/2	1/2
	B (Å^2)	0.5	0.5	0.5	0.5	0.5	0.5
	g	1.0	1.0	1.0	1.0	1.0	1.0
Sn	x	0	0	0	0	0	0
	y	0	0	0	0	0	0
	z	0	0	0	0	0	0
	B (Å^2)	0.5	0.5	0.5	0.5	0.5	0.5
	g	1.0	1.0	1.0	1.0	1.0	1.0
R_{wp} (%)		8.454	5.578	6.856	4.430	6.430	5.498
R_e (%)		1.089	0.959	1.163	0.984	1.086	0.961
S		7.7645	5.8182	5.8978	4.504	5.921	5.719

Table.2 Crystal structure parameters of Fe_2TiSn alloys and the 2nd phase of FeSn.

milling time		1h in Air		1h in Ar		3h in Air		3h in Ar		12h in Air		12h in Ar	
the 1st / 2nd phase		Fe_2TiSn / FeSn		Fe_2TiSn / FeSn		Fe_2TiSn / FeSn		Fe_2TiSn / FeSn		Fe_2TiSn / FeSn		Fe_2TiSn / FeSn	
space group		*Fm-3m*	*P 6/m m m*	*Fm-3m*	*P 6/mm m*	*Fm-3m*	*P 6/m m m*	*Fm-3m*	*P 6 /mm m*	*Fm-3m*	*P 6 /mm m*	*Fm-3m*	*P 6/m m m*
a(Å)		6.0486(4)	5.2995(9)	6.0713(5)	5.3090(5)	6.0727(0)	5.3000(8)	6.0719(2)	5.3236(9)	6.0718(0)	5.2985(4)	6.0722(7)	5.2970(0)
b(Å)		6.0486(4)	5.2995(9)	6.0713(5)	5.3090(5)	6.0727(0)	5.3000(8)	6.0719(2)	5.3236(9)	6.0718(0)	5.2985(4)	6.0722(7)	5.2970(0)
c(Å)		6.0486(4)	4.4463(4)	6.0713(5)	4.4246(0)	6.0727(0)	4.4435(5)	6.0719(2)	4.4054(7)	6.0718(0)	4.4444(8)	6.0722(7)	4.4810(0)
α(deg.)		90	90	90	90	90	90	90	90	90	90	90	90
β(deg.)		90	90	90	90	90	90	90	90	90	90	90	90
γ(deg.)		90	120	90	120	90	120	90	120	90	120	90	120
V(Å^3)		221.29(6)	108.14(7)	223.79(8)	108.00(3)	223.90(8)	107.76(4)	223.86(0)	108.13(0)	223.84(7)	108.05(9)	223.89(9)	108.884(3)
Fe	x	1/4	1/2	1/4	1/2	1/4	1/2	1/4	1/2	1/4	1/2	1/4	1/2
	y	1/4	0	1/4	0	1/4	0	1/4	0	1/4	0	1/4	0
	z	1/4	0	1/4	0	1/4	0	1/4	0	1/4	0	1/4	0
	B(Å^2)	0.5	0.5	0.5	0.5	0.5	0.5	0.5	0.5	0.5	0.5	0.5	0.5
	g	1.0	1.0	1.0	1.0	1.0	1.0	1.0	1.0	1.0	1.0	1.0	1.0
Ti	x	1/2	—	1/2	—	1/2	—	1/2	—	1/2	—	1/2	—
	y	1/2	—	1/2	—	1/2	—	1/2	—	1/2	—	1/2	—
	z	1/2	—	1/2	—	1/2	—	1/2	—	1/2	—	1/2	—
	B(Å^2)	0.5	—	0.5	—	0.5	—	0.5	—	0.5	—	0.5	—
	g	1.0	—	1.0	—	1.0	—	1.0	—	1.0	—	1.0	—
Sn1	x	0	1/3	0	1/3	0	1/3	0	1/3	0	1/3	0	1/3
	y	0	2/3	0	2/3	0	2/3	0	2/3	0	2/3	0	2/3
	z	0	1/2	0	1/2	0	1/2	0	1/2	0	1/2	0	1/2
	B(Å^2)	0.5	0.5	0.5	0.5	0.5	0.5	0.5	0.5	0.5	0.5	0.5	0.5
	g	1.0	1.0	1.0	1.0	1.0	1.0	1.0	1.0	1.0	1.0	1.0	1.0
Sn2	x	—	0	—	0	—	0	—	0	—	0	—	0
	y	—	0	—	0	—	0	—	0	—	0	—	0
	z	—	0	—	0	—	0	—	0	—	0	—	0
	B(Å^2)	—	0.5	—	0.5	—	0.5	—	0.5	—	0.5	—	0.5
	g	—	1.0	—	1.0	—	1.0	—	1.0	—	1.0	—	1.0
R_{wp}(%)		5.279		5.245		6.129		4.798		4.181		5.114	
R_e(%)		1.089		0.959		1.162		0.984		1.086		0.962	
S		4.8486		5.4704		5.7574		4.8770		3.8506		5.3175	

Table.3 Non-stoichiometric composition and VEC of Fe_2TiSn alloys.

milling time	1h in Air	1h in Ar	3h in Air	3h in Ar	12h in Air	12h in Ar
composition ratio of Fe (%)	51(4)	51(1)	50(5)	52(2)	47(5)	50(2)
composition ratio of Ti (%)	26(5)	25(2)	24(9)	25(2)	29(4)	27(2)
composition ratio of Sn (%)	23(2)	24(2)	26(5)	23(1)	24(2)	23(1)
non-stoichiometric composition	$Fe_{2.0(2)}Ti_{1.1(2)}Sn_{0.91(7)}$	$Fe_{2.05(5)}Ti_{1.00(8)}Sn_{0.94(7)}$	$Fe_{2.0(2)}Ti_{1.0(4)}Sn_{1.0(2)}$	$Fe_{2.07(6)}Ti_{1.00(8)}Sn_{0.94(5)}$	$Fe_{1.9(2)}Ti_{1.2(2)}Sn_{0.94(7)}$	$Fe_{2.01(7)}Ti_{1.09(8)}Sn_{0.90(3)}$
VEC	5.4 ～ 6.6	5.9 ～ 6.3	5.1 ～ 6.9	5.8 ～ 6.4	5.3 ～ 6.5	5.8 ～ 6.2